Note: This copy is for your personal non-commercial use only. To order presentation-ready copies for distribution to your colleagues or clients, contact us at www.rsna.org/rsnarights.

Prostate Cancer: Identification with Combined Diffusion-weighted MR Imaging and 3D ^{1}H MR Spectroscopic Imaging—Correlation with Pathologic Findings[1]

Yousef Mazaheri, PhD
Amita Shukla-Dave, PhD
Hedvig Hricak, MD, PhD
Samson W. Fine, MD
Jingbo Zhang, MD
Gloria Inurrigarro, MD
Chaya S. Moskowitz, PhD
Nicole M. Ishill, MS
Victor E. Reuter, MD
Karim Touijer, MD
Kristen L. Zakian, PhD
Jason A. Koutcher, MD, PhD

Purpose: To retrospectively measure the mean apparent diffusion coefficient (ADC) with diffusion-weighted magnetic resonance (MR) imaging and the mean metabolic ratio (MET) with three-dimensional (3D) hydrogen 1 (^{1}H) MR spectroscopic imaging in regions of interest (ROIs) drawn over benign and malignant peripheral zone (PZ) prostatic tissue and to assess ADC, MET, and combined ADC and MET for identifying malignant ROIs, with whole-mount histopathologic examination as the reference standard.

Materials and Methods: The institutional review board approved this HIPAA-compliant retrospective study and issued a waiver of informed consent. From among 61 consecutive patients with prostate cancer, 38 men (median age, 61 years; range, 42–72 years) who underwent 1.5-T endorectal MR imaging before radical prostatectomy and who fulfilled all inclusion criteria of no prior hormonal or radiation treatment and at least one PZ lesion (volume, >0.1 cm^3) at whole-mount pathologic examination were included. ADC maps were generated from diffusion-weighted MR imaging data, and MET maps of (choline plus polyamine plus creatine)/citrate were calculated from 3D ^{1}H MR spectroscopic imaging data. ROIs in the PZ identified by matching pathologic slides with T2-weighted images were overlaid on MET and ADC maps. Areas under the receiver operating characteristic curves (AUCs) were used to evaluate accuracy.

Results: The mean ADC ± standard deviation, $(1.39 \pm 0.23) \times 10^{-3}$ mm^2/sec, and mean MET (0.92 ± 0.32) for malignant ROIs differed significantly from the mean ADC, $(1.69 \pm 0.24) \times 10^{-3}$ mm^2/sec, and mean MET (0.73 ± 0.18) for benign ROIs ($P < .001$ for both). In distinguishing malignant ROIs, combined ADC and MET (AUC = 0.85) performed significantly better than MET alone (AUC = 0.74; $P = .005$) and was also better than ADC alone (AUC = 0.81), although the difference was not statistically significant ($P = .09$).

Conclusion: The combination of ADC and MET performs significantly better than MET for differentiating between benign and malignant ROIs in the PZ.

© RSNA, 2008

[1] From the Departments of Medical Physics (Y.M., A.S., K.L.Z., J.A.K.), Radiology (Y.M., A.S., H.H., J.Z., K.L.Z., J.A.K.), Pathology (S.W.F., G.I., V.E.R.), Epidemiology and Biostatistics (C.S.M., N.M.I.), and Urology (K.T.), Memorial Sloan-Kettering Cancer Center, 1275 York Ave, Room C-278, New York, NY 10021. Received February 22, 2007; revision requested April 26; revision received June 15; final version accepted July 23. Supported by National Institutes of Health grant R01 CA76423. **Address correspondence to** Y.M. (e-mail: *mazahery@mskcc.org*).

© RSNA, 2008

Magnetic resonance (MR) imaging has shown great promise as a noninvasive diagnostic tool in the evaluation and management of prostate cancer. By aiding in the detection, localization, and staging of prostate cancer (including the assessment of extracapsular extension and seminal vesicle invasion), multiplanar T2-weighted endorectal MR imaging can facilitate more appropriate treatment selection and planning. However, for distinguishing prostate cancer from nonmalignant tissue, T2-weighted MR imaging has high sensitivity but low specificity (1–3). To further improve the specificity and sensitivity of MR imaging, functional MR imaging techniques such as three-dimensional (3D) hydrogen 1 (^{1}H) MR spectroscopic imaging (4,5), dynamic contrast material–enhanced MR imaging (6–9), and diffusion-weighted imaging (10–14) have been proposed.

Three-dimensional ^{1}H MR spectroscopic imaging provides information on relative concentrations of the metabolites citrate, creatine, polyamines, and choline within a voxel. Metabolic information from 3D ^{1}H MR spectroscopic imaging has been shown to improve tumor localization and volume estimation with MR imaging and to provide valuable information about the aggressiveness of prostate cancer (15–18).

Diffusion-weighted MR imaging is a noninvasive technique that is sensitive to the structure of biologic tissue at the microscopic level. Results of several studies have suggested that apparent diffusion coefficient (ADC) values calculated from diffusion-weighted imaging data may have clinical utility in prostate cancer diagnosis. In studies of patients with biopsy-proved cancer, mean ADC values for malignant peripheral zone (PZ) (10) and transition zone (11) tissue were lower than those for nonmalignant PZ and transition zone tissue, despite sizable overlap. The addition of diffusion-weighted imaging to conventional T2-weighted MR imaging has been found to improve the detection of prostate cancer (14), and diffusion-weighted imaging at 3.0 T has demonstrated reduced ADC values and increased fractional anisotropy in prostate cancer (19).

In a study that involved both diffusion-weighted imaging and 3D ^{1}H MR spectroscopic imaging, Kumar et al (20) reported a positive correlation between ADC values and the ratio of citrate to choline and creatine in men with elevated prostate-specific antigen (PSA) levels; this correlation may reflect a direct relationship between the reduction of citrate levels and structural changes of prostate tissue associated with malignancy. More recently, Reinsberg et al (21) reported increased specificity, without a reduction in sensitivity, for combined diffusion-weighted imaging and two-dimensional ^{1}H MR spectroscopic imaging—as compared with MR spectroscopy alone or diffusion-weighted imaging alone—in voxels containing 70% or more tumorous tissue. However, in their study, tumor was defined as a low-signal-intensity region at T2-weighted imaging within a sextant that was positive for tumor at biopsy, and whole-mount step-section pathologic evaluation was not used as the standard of reference. The goals of our present study were to retrospectively measure the mean ADC with diffusion-weighted MR imaging and the mean metabolic ratio (MET) with 3D ^{1}H MR spectroscopic imaging for regions of interest (ROIs) drawn over benign and malignant PZ prostate tissue and to assess ADC, MET, and combined ADC and MET for identifying malignant ROIs, with whole-mount histopathologic examination as the reference standard.

Advances in Knowledge

- To our knowledge, ours is the first study to use combined diffusion-weighted imaging and three-dimensional (3D) hydrogen 1 (^{1}H) MR spectroscopic imaging of the prostate with whole-mount histopathologic examination as the reference standard.
- Combined diffusion-weighted and 3D ^{1}H MR spectroscopic imaging performs significantly better (P = .005) than 3D ^{1}H MR spectroscopic imaging alone for differentiating between benign and malignant regions of interest in the peripheral zone.

Implication for Patient Care

- Our study results show the potential of combined diffusion-weighted and 3D ^{1}H MR spectroscopic imaging in the identification of prostate cancer.

Materials and Methods

Our institutional review board approved and issued a waiver of informed consent for our retrospective study, which was compliant with the Health Insurance Portability and Accountability Act. Between April 2005 and September 2005, 61 consecutive patients with biopsy-proved prostate cancer who were referred for MR imaging by the urology department at our institution underwent MR imaging, 3D ^{1}H MR spectroscopic imaging, and diffusion-weighted imaging before radical prostatectomy. Thirty-eight men (median age, 61 years; age range, 42–72 years) met the following criteria for inclusion in our study: *(a)* no prior hormonal or radia-

Published online
10.1148/radiol.2462070368

Radiology 2008; 246:480–488

Abbreviations:
ADC = apparent diffusion coefficient
AUC = area under the receiver operating characteristic curve
CI = confidence interval
MET = metabolic ratio
PRESS = point-resolved spatially localized spectroscopy
PSA = prostate-specific antigen
PZ = peripheral zone
ROI = region of interest
3D = three-dimensional

Author contributions:
Guarantors of integrity of entire study, Y.M., H.H.; study concepts/study design or data acquisition or data analysis/interpretation, all authors; manuscript drafting or manuscript revision for important intellectual content, all authors; manuscript final version approval, all authors; literature research, A.S.; clinical studies, Y.M., A.S., H.H., S.W.F., K.L.Z., J.A.K.; experimental studies, G.I.; statistical analysis, N.M.I.; and manuscript editing, Y.M., A.S., H.H., S.W.F., N.M.I., K.L.Z., J.A.K.

Authors stated no financial relationship to disclose.

tion treatment and *(b)* at least one PZ lesion with volume greater than 0.1 cm^3 at whole-mount pathologic examination. The mean serum PSA level for the cohort was 5.94 ng/mL (range, 0.58–21.29 ng/mL), with a median value of 5.53 ng/mL. Thirty-five patients (92%) had a Gleason score at surgery of 7 or lower (Table 1). In addition, a large majority of patients (30 of 38 [79%]) had disease with a clinical stage of T1c (Table 1). The median Gleason score at surgical pathologic examination was 7 (range, 6–9).

MR Imaging

MR imaging studies were performed with a 1.5-T whole-body MR imaging unit (Signa Horizon; GE Medical Systems, Milwaukee, Wis). A body coil was used for excitation, and a pelvic four-channel phased-array coil combined with a commercially available balloon-covered expandable endorectal coil (Medrad, Pittsburgh, Pa) was used for signal reception. Transverse T1-weighted images (repetition time msec/echo time msec, 400–700/10–14; section thickness, 5 mm; intersection gap, 0 mm; field of view, 24–26 cm; and matrix, 256 × 192) and transverse, coronal, and sagittal T2-weighted fast spin-echo images (4400/102 [effective]; echo train length, 12; section thickness, 3 mm; intersection gap, 0 mm; field of view, 14 cm; and matrix, 256 × 192) of the prostate and seminal vesicles were obtained.

Diffusion-weighted Imaging

Diffusion-weighted images were obtained by using single-shot spin-echo echo-planar imaging with a pair of rectangular gradient pulses along three orthogonal axes. The imaging parameters were as follows: 4000/99.8; field of view, 14 × 14 cm^2; section thickness, 3 mm; intersection gap, 0 mm; and in-plane resolution, 1.9 × 1.9 mm^2 (matrix, 72 × 72). Images were zero-filled to a 256 × 256 matrix. The orientation and location of these images were prescribed identically to the transverse T2-weighted prostate images. The *b* values were 0 and 800 sec/mm^2. From four to eight images were averaged, and the duration of the diffusion-weighted imaging component of the examination was about 4 minutes. Typically, 11–18 sections were acquired to cover the whole prostate.

In the presence of diffusion sensitizing gradients, the ADC is given by the following equation:

$$\mathrm{ADC} = \frac{-1}{b}\ln\left(\frac{S(b)}{S(0)}\right), \qquad (1)$$

where $S(b)$ and $S(0)$ are the signal intensities of each voxel with and without diffusion weighting, respectively, and b is the diffusion-sensitizing factor (b value). ADC maps were constructed according to Equation (1) on the basis of a voxel-wise calculation and were interpolated to a 256 × 256 matrix.

Three-dimensional ^{1}H MR Spectroscopic Imaging

Three-dimensional ^{1}H MR spectroscopic imaging was performed with a commercially available acquisition package (PROSE [PROstate Spectroscopy and Imaging Examination]; GE Medical Systems). The PROSE sequence acquires data with the point-resolved spatially localized spectroscopy (PRESS) technique by using spectral-spatial pulses (22) to excite choline, polyamines, creatine, and citrate within the PRESS box while water and lipids are suppressed. The PRESS box was positioned on transverse T2-weighted images by an MR imaging technologist with the supervision of a physicist (A.S., with more than 5 years of experience in prostate spectroscopy) to maximize coverage of the prostate while minimizing inclusion of periprostatic fat. Further reduction of water and lipid contamination was achieved by using very selective outer voxel suppression pulses, which confine the PRESS selection more closely to the shape of the prostate (23). Magnetic field homogeneity was optimized for the selected volume by using an automated shimming algorithm provided by the manufacturer. Further shimming was performed manually, if necessary, to further reduce the line width. The 3D MR spectroscopic imaging parameters were as follows: 1000/130; number of signals acquired, one; spectral width, 1250 Hz; number of points, 512; field of view, 11 × 5.5 × 5.5 cm^3; and 16 × 8 × 8 phase-encoding steps. The MR spectroscopic imaging acquisition voxel volume was 326.1 mm^3. The duration for this component of the examination was 17 minutes. The total examination time, including conventional T1- and T2-weighted imaging, diffusion-weighted imaging, and 3D ^{1}H MR spectroscopic imaging, was about 1 hour, which included time for coil placement, patient positioning, and localization of the prostate.

Spectral data were processed by using the manufacturer's postprocessing software package. Processing included zero-filling of the raw data in the superoinferior direction and reconstruction with a four-dimensional Fourier transformation to yield a voxel volume of 160 mm^3, spectral apodization with a 2-Hz Lorentzian function, baseline correction, peak registration, and alignment of 3D ^{1}H MR spectroscopic images to the transverse T2-weighted MR images. Estimates of the areas under the resonances of the metabolite peaks were obtained by integrating a region centered at each peak. The diam-

Table 1

Distribution of Characteristics in 38 Patients

Characteristic	Frequency
Gleason score at biopsy	
6 (3 + 3)	17 (45)
7 (3 + 4)	11 (29)
7 (4 + 3)	8 (21)
9 (4 + 5)	2 (5)
Gleason score at surgery	
6 (3 + 3)	12 (32)
7 (3 + 4)	16 (42)
7 (4 + 3)	7 (18)
9 (4 + 5)	3 (8)
Clinical stage	
T1c	30 (79)
T2a	5 (13)
T2c	1 (3)
T3a	2 (5)

Note.—Data are numbers of patients, with percentages in parentheses.

eter of integration was 0.3 ppm but was adjusted slightly for each voxel to best account for the broadening of the spectral peak. Metabolic ratio maps of (choline plus polyamine plus creatine)/citrate were generated.

Pathologic Evaluation and Image Correlation

The specimen was step sectioned after prostate resection, as previously described (24). The cancer foci were outlined in ink on whole-mount step-section pathologic slices of the prostate before being photographed. A radiologist (J.Z., with 4 years of experience) in conjunction with two pathologists (S.W.F. and V.E.R., with 30 years of combined experience) evaluated the pathologic maps and the MR images during four dedicated sessions focused on matching whole-mount step-section pathologic slices with the corresponding T2-weighted images. The most closely corresponding transverse T2-weighted images and pathologic step-section slices were paired on the basis of anatomic landmarks, including the presence of urinary bladder and seminal vesicle tissue in superior imaging sections; the largest prostate diameter and progressive changes in the prostate diameter; the thickness of the PZ and the position of the pseudocapsule; and the presence, size, and shape of the transition zone. With both the pathology maps and MR images displayed, the largest possible round or elliptical ROI was placed on the PZ tumor on the T2-weighted images, avoiding tumor edges and regions containing postbiopsy hemorrhage, benign tissue, the prostate capsule, or the urethra. A corresponding ROI of the same size as that used for the tumor was drawn on the opposite side of the sextant where there was no indication of prostate cancer on the pathology slides.

The ROIs drawn on T2-weighted images by using whole-mount step-section histopathologic findings were mapped on the 3D ^{1}H MR spectroscopic imaging grid for voxel selection and on the ADC map for drawing ROIs. The radiologist did not draw ROIs for tumor foci that were 0.1 cm^3 or smaller, as this would have introduced bias because of the partial volume effect. On the 3D ^{1}H MR spectroscopic imaging grid, the ROI consisted of all voxels that contained more than 60% tumor tissue on the basis of comparison of the grid with T2-weighted images. When a tumor corresponded to more than a single MR spectroscopic imaging voxel, an equal number of voxels was selected from among the correlating benign MR spectroscopic imaging voxels.

Outer-volume signal bleed and ghosts (potentially due to patient motion) were the basis for voxel rejection. Signal-to-noise ratio was not used as a criterion for rejection of voxels. Four of 61 patients (7%) were excluded from the study because their spectroscopic imaging data were deemed unusable. A corresponding ROI was drawn on the ADC map. Because of the one-to-one correspondence of the ADC voxels to the voxels of the T2-weighted images, the partial volume effect was minimized when ROIs were drawn on the ADC maps on the basis of T2-weighted images. Small adjustments were made in the location of the ROI in the ADC map if the image appeared distorted because of susceptibility artifacts.

The orientations of T2-weighted, diffusion-weighted, and 3D ^{1}H MR spectroscopic imaging techniques were identical; hence, there was direct correspondence for each section in the absence of patient motion. The inherent differences in image size (field of view) and through-plane coverage (number of sections) of the T2-weighted, diffusion-weighted, and 3D ^{1}H MR spectroscopic imaging data were adjusted manually at a workstation (Advantage Windows; GE Medical Systems).

Statistical Analysis

Analyses were performed with software (Intercooled Stata, version 9.0 for Windows, 2005, Stata, College Station, Tex; and S-Plus, version 7.0 for Windows, 2005, Insightful, Seattle, Wash). The units of analysis were mean ADC and mean MET for each multivoxel ROI. The mean values of the benign ROIs were compared with the mean values of the malignant ROIs by using paired *t* tests. Diffusion-weighted information and 3D ^{1}H MR spectroscopic imaging information were combined by using generalized estimating equations with an independence working correlation matrix to account for the correlated data. To obtain predicted probabilities of an ROI being cancerous, the mean ADC and the mean MET for the ROI were entered into a logistic regression model. On the basis of the results of this model (Table 2), we obtained the following equation for the probability of an ROI being cancerous:

$$\exp(4.3 - 5123.5 \cdot \mathrm{ADC} + 4.5 \cdot \mathrm{MET}) / [1 + \exp(4.3 - 5123.5 \cdot \mathrm{ADC} + 4.5 \cdot \mathrm{MET})]. \quad (2)$$

The regression model yielded estimated regression coefficients that weighted the information from these two variables in an optimal way for combining them. The regression analysis also determined whether each variable was significantly associated with the probability of an ROI being cancerous, after adjusting for the other information.

Receiver operating characteristic curves and the corresponding areas under the receiver operating characteris-

Table 2

Regression Model for Combining Diffusion-weighted and 3D ^{1}H MR Spectroscopic Imaging Information

Parameter	Regression Coefficient*	*P* Value
Mean ADC value	−5123.5 (−7182.7, −3064.3)	<.001
Mean MET	4.5 (1.45, 7.55)	.004

Note.—Values were obtained from a logistic regression model with an estimated intercept parameter of 4.3.

* Data in parentheses are 95% confidence intervals (CIs).

tic curves (AUCs) were estimated nonparametrically for the detection of cancer by using mean ADC, mean MET, and combined mean ADC and mean MET values for each ROI. In all statistical methods, a P value of less than .05 was considered to indicate a significant difference. Because smaller ADC values are associated with cancer, for the receiver operating characteristic analysis we transformed the ADC value by multiplying it by −1. To adjust for the correlated data, the standard errors and comparisons between AUCs were calculated by using the methods of Obuchowski (25). To produce a bias-corrected estimate of the AUC for the logistic regression model (to compensate for the fact that the model was evaluated by using the same data from which it was built), we used a bootstrap approach to resample patients (26).

Results

A total of 244 malignant and 244 benign spectroscopic voxels (median number of voxels per patient, 5; range, 1–41) were used in the analysis. A total of 127 benign and 127 malignant ROIs were used. The median number of benign ROIs per patient was three (range, one to nine), and the median number of malignant ROIs per patient was three (range, 1:9). The mean ADC values for benign and malignant ROIs in the PZ overlapped substantially (Fig 1a), as did mean MET values (Fig 1b).

The mean ADC value for all patients for malignant ROIs in the PZ (mean ± standard deviation, [1.39 ± 0.23] × 10^{-3} mm^2/sec) was significantly lower than that for benign ROIs in the PZ ([1.69 ± 0.24] × 10^{-3} mm^2/sec) ($P <$ .001) (Table 3). The mean MET for all patients for malignant ROIs in the PZ (0.92 ± 0.32) was significantly higher than that for benign ROIs in the PZ (0.73 ± 0.18) ($P <$ .001) (Table 3).

In differentiating malignant from benign ROIs in the PZ, the combination of ADC and MET (AUC = 0.85; 95% CI: 0.72, 0.97) was significantly more accurate than MET alone (AUC = 0.74; 95% CI: 0.62, 0.85; P = .005) (Fig 2) and was also more accurate than ADC alone (AUC = 0.81; 95% CI: 0.71, 0.90), although the latter difference was not significant (P = .09). ADC alone had slightly higher accuracy than MET alone, but the difference was not significant (P = .30) (Fig 2). The deviance of the linear regression model for combined ADC and MET was 71.1 with 76 degrees of freedom, suggesting that the model fit the data reasonably well.

A representative large tumor (total tumor volume, 7.38 × 10^3 mm^3 as measured on pathology maps) was clearly depicted at MR imaging, diffusion-weighted imaging, and 3D ^{1}H MR spectroscopic imaging (Fig 3). The combination of diffusion-weighted imaging and 3D ^{1}H MR spectroscopic imaging helped to identify a representative small tumor

Figure 1

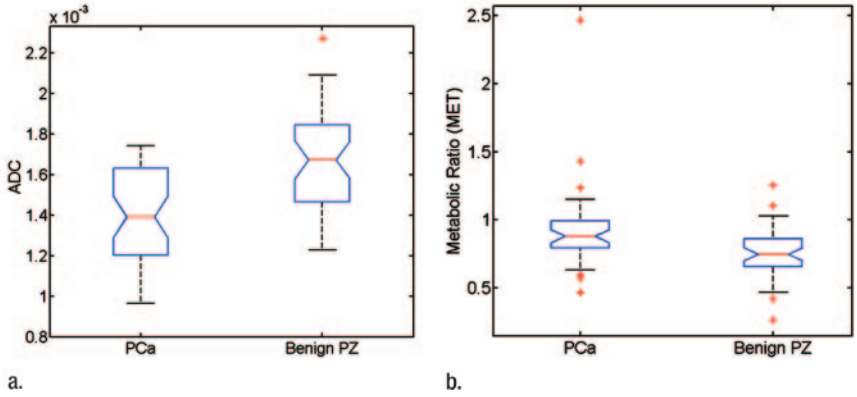

Figure 1: Box-and-whisker plots of **(a)** mean ADC (in square millimeters per second) and **(b)** mean MET in prostate cancer *(PCa)* and benign PZ ROIs from 38 patients. The mean ADC and MET values overlap substantially for benign and malignant ROIs in the PZ. Red lines = median values.

Table 3

Descriptive Statistics of ADC, MET, and Tumor Volume Measurements at Pathologic Examination

Parameter	Mean
ADC (× 10^{-3} mm^2/sec)	
Tumor ROI	1.39 (0.97–1.74)
Benign ROI	1.69 (1.23–2.27)
MET	
Tumor ROI	0.92 (0.46–2.46)
Benign ROI	0.73 (0.26–1.10)
Volume of voxels used at MR spectroscopic imaging analysis (cm^3)	0.72 (0.16–6.59)
Tumor volume on pathology slides (cm^3)	0.55 (0.12–7.38)

Note.—Data in parentheses are ranges.

Figure 2

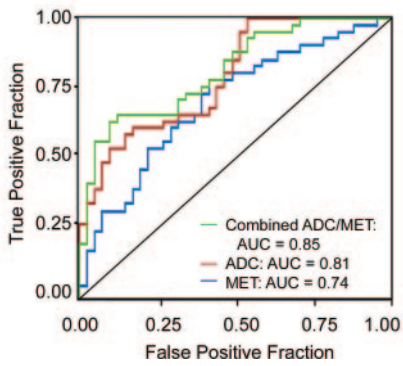

Figure 2: Receiver operating characteristic curves show ability of mean ADC alone (AUC = 0.81; 95% CI: 0.71, 0.90), mean MET alone (AUC = 0.74; 95% CI: 0.62, 0.85), and combined ADC and MET (AUC = 0.85; 95% CI: 0.72, 0.97) to differentiate between tumor and benign ROIs.

(total tumor volume, 557.95 mm^3 as measured on pathology maps) (Fig 4).

Discussion

We found that mean ADC values were significantly lower ($P < .001$) and mean MET values were significantly higher ($P < .001$) for malignant PZ tissue than for benign PZ tissue. Furthermore, the AUC for the combination of ADC and MET (0.85) was significantly higher than that for MET alone (0.74; $P = .005$) in the detection of prostate cancer.

The decrease in ADC values in malignant tissue is attributed to histopathologic characteristics, including hypercellularity, enlargement of nuclei, hyperchromatisms, and angulation of the nuclear contour (27), that result in a reduction of diffusional displacement of water molecules. Mulkern et al (28) reported bioexponential characterization of prostate tissue over an extended range of *b* values (≤3500 sec/mm^2). In our study, *b* values of 0 and 800 sec/mm^2 were used. Extending the analysis to include higher *b* values could provide better characterization of prostate cancer and specific criteria for assessing the response of prostate cancer to treatment (29,30). Gibbs et al (19) noted significant differences in mean fractional anisotropy measured with diffusion-tensor imaging between prostate cancer and healthy-appearing PZ tissue at 3 T that might further help differentiate prostate cancer at higher field strengths.

To our knowledge, ours is the first study to use whole-mount histopathologic examination as the reference standard for evaluating combined diffusion-weighted and 3D ^{1}H MR spectroscopic imaging for prostate cancer

Figure 3

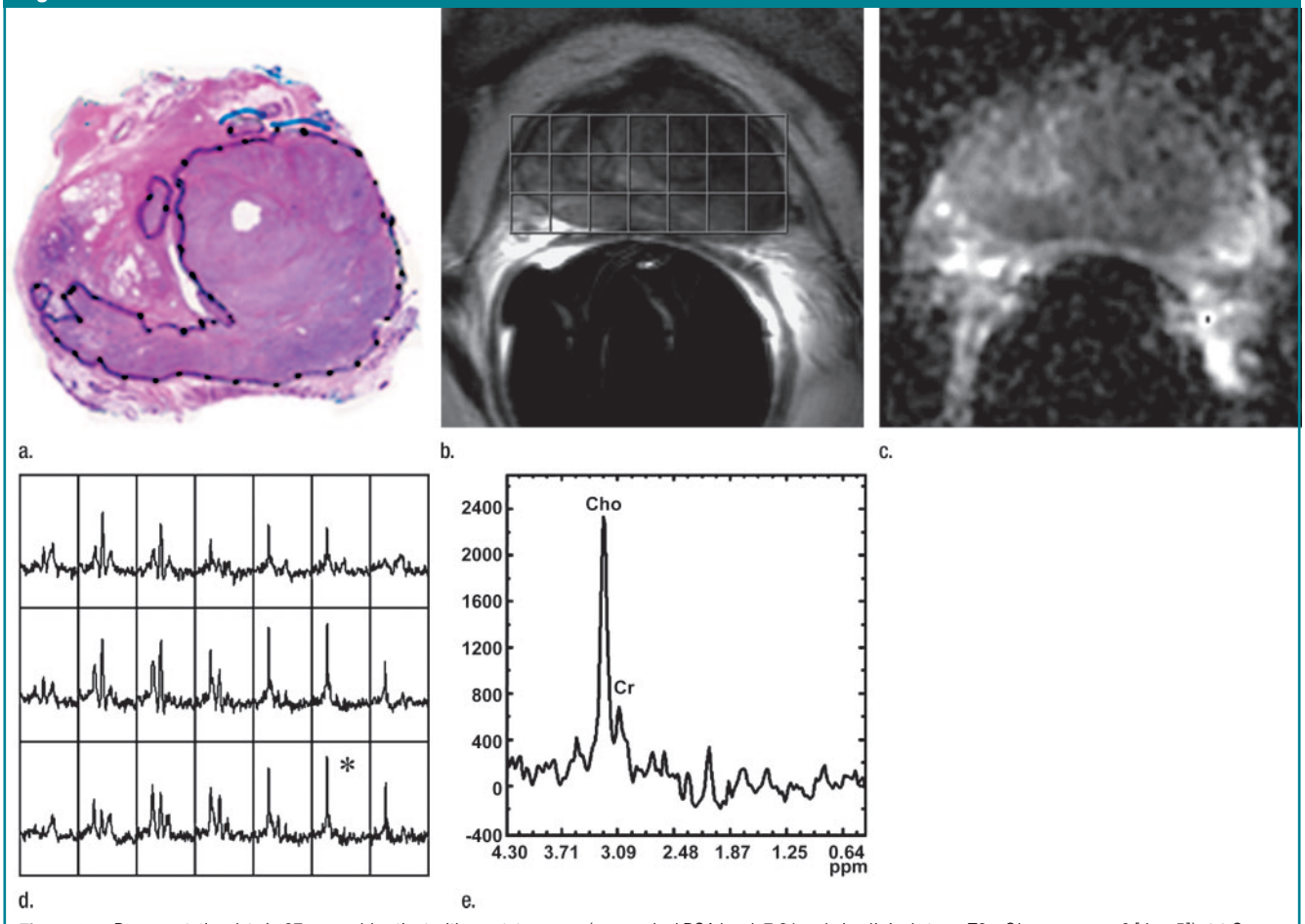

Figure 3: Representative data in 67-year-old patient with prostate cancer (presurgical PSA level, 7.21 ng/mL; clinical stage, T3a; Gleason score, 9 [4 + 5]). **(a)** On whole-mount step-section histopathologic map of prostate gland, black area represents area of Gleason grade 5 cancer. (Hematoxylin-eosin stain.) **(b)** Transverse T2-weighted MR image (4400/102 [effective]) closest to histopathologic map shows tumor as focal region of reduced signal intensity in the PZ. Overlaid box indicates PRESS excitation region selected for 3D ^{1}H MR spectroscopic imaging. **(c)** ADC map of same section as in **b,** generated by using diffusion-weighted MR images (4000/99.8) at *b* values of 0 and 800 sec/mm^2. **(d, e)** Three-dimensional ^{1}H MR spectroscopic imaging data set (1000/130) **(d)** of same section as in **b** shows **(e)** voxel in PZ (∗ in **d**) with elevated (choline *[Cho]* plus polyamine plus creatine *[Cr]*)/citrate ratio that is suspicious for cancer. Voxel sizes of the T2-weighted, diffusion-weighted, and 3D ^{1}H MR spectroscopic imaging data sets were 1.2, 10.8, and 160 mm^3, respectively.

Figure 4

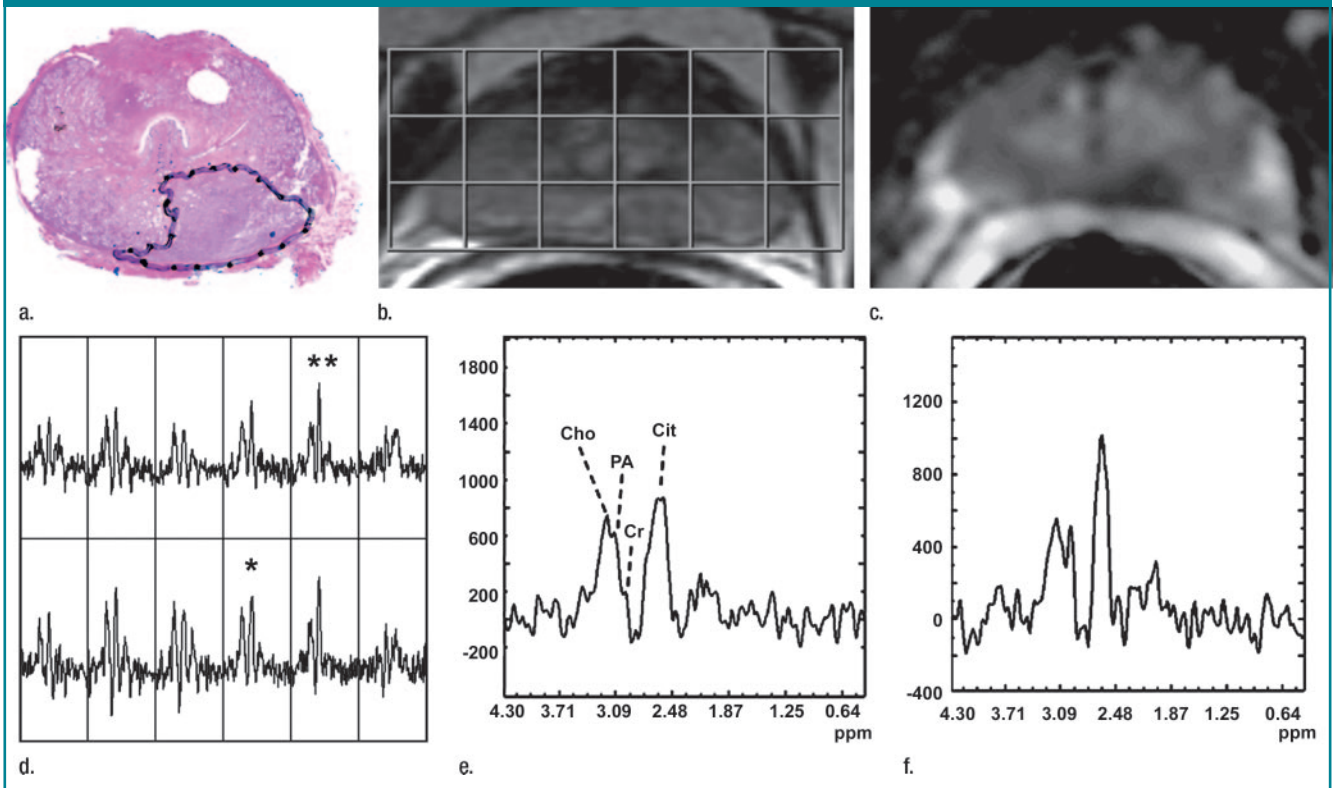

Figure 4: Representative data in 44-year-old patient with prostate cancer (presurgical PSA level, 9.43 ng/mL; clinical stage, T1c; surgical Gleason score, 7 [4 + 3]). **(a)** Whole-mount step-section histopathologic map. (Hematoxylin-eosin stain.) **(b)** Closest transverse T2-weighted image (4400/102) and overlaid PRESS box indicating excitation region selected for 3D ^{1}H MR spectroscopic imaging. **(c)** ADC map of same section as in **b**. **(d–f)** Three-dimensional ^{1}H MR spectroscopic imaging data set (1000/130) **(d)** of PRESS box in **b** shows **(e)** voxel in PZ (∗ in **d**) with elevated (choline *[Cho]* plus polyamine *[PA]* plus creatine *[Cr]*)/citrate *(Cit)* ratio that is suspicious for cancer and **(f)** healthy-appearing voxel (∗∗ in **d**) that contains high levels of citrate.

detection. This is important, as tumor localization and assessment of surgical Gleason score in the prostate can only be conclusively determined on the basis of step-section pathologic analysis after radical prostatectomy. In our study, the surgical Gleason score differed from the biopsy Gleason score for many patients. In addition, although patients selected for our study were consecutive patients referred for MR imaging by the urology department at our institution who satisfied the inclusion criteria of the study, their key clinical features, including age, PSA level, surgical Gleason score (32% of the patients had a Gleason score of 6), and clinical disease stage were consistent with the general trend of downstaging of prostate cancer. Therefore, our study addresses the challenges faced in current clinical practice and shows the potential of diffusion-weighted and 3D ^{1}H MR spectroscopic imaging to assist in diagnosis.

Furthermore, although we coregistered the ADC and MET maps in our analysis, we did not resample the ADC map to match the MET map, preserving the original higher spatial resolution of diffusion-weighted imaging. Our analysis is limited to an ROI-based comparison and does not include the voxel-by-voxel comparison used in some other studies (20,21), but our approach takes full advantage of the higher spatial resolution of diffusion-weighted imaging to limit the partial volume effect by delineating the ROIs on the basis of the T2-weighted images. Finally, as compared with the two-dimensional ^{1}H MR spectroscopic imaging technique used in a similar study by Reinsberg et al (21), the 3D ^{1}H MR spectroscopic imaging acquisition technique used in our study provides higher spatial resolution in the through-plane direction and, therefore, greater sensitivity for small tumor volumes.

Our mean ADC results fall within the wide range of values that have been previously reported for benign and malignant prostate tissue in the PZ (10–14). The variation in reported values could be due to a number of physiologic factors (eg, age, tumor grade, tumor size) as well as technical factors (eg, variations in acquisition parameters and postprocessing methods).

Our study had limitations. First, MR imaging artifacts were potential sources of error in our measurements. Diffusion-weighted imaging artifacts include white pixel noise, low signal-to-noise ra-

tio, and susceptibility artifacts. Three-dimensional ^{1}H MR spectroscopic imaging artifacts include lipid contamination and susceptibility artifacts. Physiologic and patient motion during imaging can also introduce artifacts, including broadening of the spectral line width and reduction in the accuracy of ROI registration. Improvements can be expected with the use of methods that offer a reduction of image distortion and increased field strength to improve signal-to-noise ratio.

Second, this study provides only a retrospective analysis of combined diffusion-weighted and 3D ^{1}H MR spectroscopic imaging to differentiate PZ prostate cancer from benign PZ tissue. The standard clinical practice includes T2-weighted imaging as a key component for clinical diagnosis. Our study was limited to looking at diffusion-weighted and 3D ^{1}H MR spectroscopic imaging to determine the potential utility of diffusion-weighted imaging or combined diffusion-weighted and 3D ^{1}H MR spectroscopic imaging for the detection of cancer. To establish the clinical utility of the proposed methods, a prospective study should be done that combines T2-weighted MR imaging with the clinical evaluation of the probability of cancer as determined by our regression model and that uses whole-mount pathologic analysis as the standard of reference.

Third, because of the discrepancy in voxel size, the voxels of the ROIs on the ADC maps did not correspond exactly to the voxels of the ROIs on the MET maps. Spectroscopic techniques that increase spatial resolution without increasing imaging duration (31) could reduce discrepancies in voxel size and allow voxel-by-voxel analysis.

In our study, combined diffusion-weighted and 3D ^{1}H MR spectroscopic imaging was not significantly more accurate than diffusion-weighted imaging alone in identifying cancer (P = .09). However, we hypothesize that with increased MR spectroscopic imaging spatial resolution, the combination of 3D ^{1}H MR spectroscopic imaging and diffusion-weighted imaging might provide significantly higher accuracy in tumor detection than either technique alone. There is a considerable difference between the spatial resolution of 3D ^{1}H MR spectroscopic imaging (160 mm^{3}) and that of diffusion-weighted imaging (10.8 mm^{3}) with our 1.5 T system; indeed, the spatial resolution of 3D ^{1}H MR spectroscopic imaging is approximately 15 times lower than that of diffusion-weighted imaging. Increased field strength and more efficient acquisition sequences would improve the signal-to-noise ratio, making 3D ^{1}H MR spectroscopic imaging with high spatial resolution feasible (32). In turn, this would increase the sensitivity and overall accuracy of 3D ^{1}H MR spectroscopic imaging for the detection of small tumors and serve the larger objective of our research, which is to be able to distinguish low-risk, localized prostate cancers and improve treatment selection (33). Furthermore, the numerous advantages of spectroscopic imaging reported in the literature, which include correlation with Gleason score and tumor response to therapy, are enough to warrant the use of 3D ^{1}H MR spectroscopic imaging in addition to diffusion-weighted imaging of the prostate.

In conclusion, the combination of diffusion-weighted and 3D ^{1}H MR spectroscopic imaging is a promising approach for discriminating between benign and malignant ROIs in the PZ.

Acknowledgment: We are grateful to Ms. Ada Muellner, BA, for helping to edit this manuscript.

References

1. Ikonen S, Kivisaari L, Tervahartiala P, Vehmas T, Taari K, Rannikko S. Prostatic MR imaging: accuracy in differentiating cancer from other prostatic disorders. Acta Radiol 2001;42:348–354.
2. Hricak H, White S, Vigneron D, et al. Carcinoma of the prostate gland: MR imaging with pelvic phased-array coils versus integrated endorectal-pelvic phased-array coils. Radiology 1994;193:703–709.
3. Yu KK, Hricak H. Imaging prostate cancer. Radiol Clin North Am 2000;38:59–85, viii.
4. Kurhanewicz J, Vigneron DB, Hricak H, Narayan P, Carroll P, Nelson SJ. Three-dimensional H-1 MR spectroscopic imaging of the in situ human prostate with high (0.24-0.7-cm3) spatial resolution. Radiology 1996; 198:795–805.
5. Heerschap A, Jager GJ, van der Graaf M, et al. In vivo proton MR spectroscopy reveals altered metabolite content in malignant prostate tissue. Anticancer Res 1997;17: 1455–1460.
6. Turnbull LW, Buckley DL, Turnbull LS, Liney GP, Knowles AJ. Differentiation of prostatic carcinoma and benign prostatic hyperplasia: correlation between dynamic Gd-DTPA-enhanced MR imaging and histopathology. J Magn Reson Imaging 1999;9: 311–316.
7. Padhani AR, Gapinski CJ, Macvicar DA, et al. Dynamic contrast enhanced MRI of prostate cancer: correlation with morphology and tumour stage, histological grade and PSA. Clin Radiol 2000;55:99–109.
8. Noworolski SM, Henry RG, Vigneron DB, Kurhanewicz J. Dynamic contrast-enhanced MRI in normal and abnormal prostate tissues as defined by biopsy, MRI, and 3D MRSI. Magn Reson Med 2005;53:249–255.
9. Futterer JJ, Heijmink SW, Scheenen TW, et al. Prostate cancer localization with dynamic contrast-enhanced MR imaging and proton MR spectroscopic imaging. Radiology 2006;241:449–458.
10. Hosseinzadeh K, Schwarz SD. Endorectal diffusion-weighted imaging in prostate cancer to differentiate malignant and benign peripheral zone tissue. J Magn Reson Imaging 2004;20:654–661.
11. Sato C, Naganawa S, Nakamura T, et al. Differentiation of noncancerous tissue and cancer lesions by apparent diffusion coefficient values in transition and peripheral zones of the prostate. J Magn Reson Imaging 2005;21:258–262.
12. Issa B. In vivo measurement of the apparent diffusion coefficient in normal and malignant prostatic tissues using echo-planar imaging. J Magn Reson Imaging 2002;16:196–200.
13. Gibbs P, Tozer DJ, Liney GP, Turnbull LW. Comparison of quantitative T2 mapping and diffusion-weighted imaging in the normal and pathologic prostate. Magn Reson Med 2001;46:1054–1058.
14. Shimofusa R, Fujimoto H, Akamata H, et al. Diffusion-weighted imaging of prostate cancer. J Comput Assist Tomogr 2005;29:149–153.
15. Scheidler J, Hricak H, Vigneron DB, et al. Prostate cancer: localization with three-dimensional proton MR spectroscopic imaging—clinicopathologic study. Radiology 1999;213:473–480.
16. Kurhanewicz J, Swanson MG, Nelson SJ, Vigneron DB. Combined magnetic resonance imaging and spectroscopic imaging approach to molecular imaging of prostate

cancer. J Magn Reson Imaging 2002;16:451–463.

17. Zakian KL, Sircar K, Hricak H, et al. Correlation of proton MR spectroscopic imaging with Gleason score based on step-section pathologic analysis after radical prostatectomy. Radiology 2005;234:804–814.
18. Coakley FV, Kurhanewicz J, Lu Y, et al. Prostate cancer tumor volume: measurement with endorectal MR and MR spectroscopic imaging. Radiology 2002;223:91–97.
19. Gibbs P, Pickles MD, Turnbull LW. Diffusion imaging of the prostate at 3.0 tesla. Invest Radiol 2006;41:185–188.
20. Kumar V, Jagannathan NR, Kumar R, et al. Correlation between metabolite ratios and ADC values of prostate in men with increased PSA level. Magn Reson Imaging 2006;24:541–548.
21. Reinsberg SA, Payne GS, Riches SF, et al. Combined use of diffusion-weighted MRI and 1H MR spectroscopy to increase accuracy in prostate cancer detection. AJR Am J Roentgenol 2007;188:91–98.
22. Schricker AA, Pauly JM, Kurhanewicz J, Swanson MG, Vigneron DB. Dualband spectral-spatial RF pulses for prostate MR spectroscopic imaging. Magn Reson Med 2001; 46:1079–1087.
23. Tran TK, Vigneron DB, Sailasuta N, et al. Very selective suppression pulses for clinical MRSI studies of brain and prostate cancer. Magn Reson Med 2000;43:23–33.
24. Yossepowitch O, Sircar K, Scardino PT, et al. Bladder neck involvement in pathological stage pT4 radical prostatectomy specimens is not an independent prognostic factor. J Urol 2002;168:2011–2015.
25. Obuchowski NA. Nonparametric analysis of clustered ROC curve data. Biometrics 1997; 53:567–578.
26. Efron B, Tibshirani RJ. An introduction to the bootstrap. New York, NY: Chapman & Hall, 1993.
27. Anderson JR. Muir's textbook of pathology. London, England: Edward Arnold, 1985.
28. Mulkern RV, Barnes AS, Haker SJ, et al. Biexponential characterization of prostate tissue water diffusion decay curves over an extended b-factor range. Magn Reson Imaging 2006;24:563–568.
29. Chenevert TL, Meyer CR, Moffat BA, et al. Diffusion MRI: a new strategy for assessment of cancer therapeutic efficacy. Mol Imaging 2002;1:336–343.
30. Roth Y, Tichler T, Kostenich G, et al. High-b-value diffusion-weighted MR imaging for pretreatment prediction and early monitoring of tumor response to therapy in mice. Radiology 2004;232:685–692.
31. Scheenen TW, Klomp DW, Roll SA, Futterer JJ, Barentsz JO, Heerschap A. Fast acquisition-weighted three-dimensional proton MR spectroscopic imaging of the human prostate. Magn Reson Med 2004;52:80–88.
32. Chen AP, Cunningham CH, Kurhanewicz J, et al. High-resolution 3D MR spectroscopic imaging of the prostate at 3 T with the MLEV-PRESS sequence. Magn Reson Imaging 2006;24:825–832.
33. Shukla-Dave A, Hricak H, Kattan MW, et al. The utility of magnetic resonance imaging and spectroscopy for predicting insignificant prostate cancer: an initial analysis. BJU Int 2007;99:786–793.